Check for updates

Additive manufacturing of high-strength multiphase nanostructures in the binary Ni–Nb system for the discovery of new types of superalloys

M. R. Jones[1], F. W. DelRio[1], J. W. Pegues[1], P. Lu[1], R. Puckett[1], N. S. Bobbitt[1], T. J. Hardin[1], M. Chandross[1], A. B. Kustas[1], N. Argibay[1,a)

[1] Sandia National Laboratories, Material, Physical, and Chemical Sciences Center, Albuquerque, NM 87123, USA
a) Address all correspondence to this author. e-mail: nargiba@sandia.gov

Ni-based superalloys have been studied extensively due to their impressive mechanical properties, including strength and creep resistance at high temperatures. Growing interest surrounding additive manufacturing (AM) methods has led to recent investigations of alloys that are traditionally difficult to process, including Ni-based superalloys. Recent work has shown that AM methods enable high-throughput materials discovery and optimization of difficult- or impractical-to-process alloys, including those with high or even majority refractory element compositions. This work focuses on AM-enabled investigations of composition-dependent mechanical and microstructural properties for Ni–Nb binary alloys. Specifically, we report on the mechanical behavior of compositionally-graded Ni_xNb_{1-x} and uniform composition $Ni_{59.5}Nb_{40.5}$ specimens made with AM. The AM fabrication process resulted in extraordinarily high strength, attributed to the formation of a dual-phase microstructure consisting of δ-Ni_3Nb and μ-Ni_6Nb_7 intermetallic compounds with nanostructured and multimodal grain size and eutectic lamellar spacing.

Introduction

The search for new processing routes that enable fabrication of higher-temperature structural materials is an active area of research, motivated by a desire to improve energy efficiency in applications like the design of turbine engines and generators. The efficiency of these devices is proportional to the operating temperature of the fluid medium, which is limited by the high-temperature mechanical properties of available materials, including yield strength, fracture toughness, and creep resistance [1–4]. Ni-based superalloys represent the current state-of-the-art for high temperature materials, enabling operation of turbines at temperatures as high as 800 °C. These alloys derive their strength from a combination of precipitates, like face-centered cubic (FCC) γ'-Ni_3Al ($L1_2$ Strukturbericht designation) and metastable tetragonal γ''-Ni_3Nb ($D0_{22}$) intermetallic compounds in a γ-Ni-rich FCC solid-solution strengthened matrix phase, as found in Inconel alloys [5–8]. At low homologous temperatures, stresses and strain rates, deformation accommodation via microtwinning is observed in Ni-based alloys [9].

The addition of refractory metals in dilute amounts has been used to improve the strength of Ni-based superalloys at higher temperatures [10]. However, processability of alloys with large fractions of intermetallic phases, which can have extraordinary strength at high temperature but are typically brittle at low temperature, remains a significant obstacle [11]. Refractory-based superalloys, with significantly higher melting temperatures and higher specific strengths (i.e., ratio of strength-to-density), are a tantalizing prospect, though processing is extremely challenging or simply impractical using traditional methods like casting and hot- and cold-working processes [12–18].

The advent and rapid evolution of laser- and electron beam-based additive manufacturing (AM) methods has introduced new opportunities for fabrication of conventionally difficult-to-process alloys [19–23]. There are now many examples of AM-based fabrication of brittle alloys for turbine engines [20, 24–27], including Ti–Al [28], Ni-based superalloys [29–31], refractory high-entropy alloys [26, 32–35], and metallic glasses [36–38]. In this work, we investigated AM-fabrication of the Ni–Nb binary alloy across

composition space, including the glass-forming near-eutectic composition $Ni_{59.5}Nb_{40.5}$, as well as near-eutectic compositions consisting of stable but brittle dual-phase δ-Ni_3Nb ($D0_a$) and μ-Ni_6Nb_7 ($D8_5$) intermetallic structures. We demonstrate microstructural tunability using both graded and uniform composition specimens. Specimens were fabricated using a laser beam directed energy deposition (LB-DED) system, with a mixed powder stream fed from independent powder reservoirs filled with elemental Ni and Nb powders, enabling in-situ, dynamic alloying. This approach was used to generate flat compact metallurgical specimens that were compositionally graded from pure Ni to pure Nb, and a uniform near-eutectic composition. The latter resulted in the formation of a dual-phase intermetallic structure, consisting of orthorhombic δ-Ni_3Nb and hexagonal close-packed (rhombohedral) μ-Ni_6Nb_7 with multimodal phase sizes and lamellar spacing. The microstructure included nanoscale phases similar to those found in arc melted Fe–Nb eutectic alloys [39] and micro/macro-scale precipitates like those found in Ni-based superalloys [40, 41].

Hardness values up to 13 GPa were measured, exceeding the highest values reported for bulk nanocrystalline metals and structural alloys [40, 42–45]. Scratch-based [46] and nanoindentation [47] methods were used to measure hardness and fracture toughness on both specimens to rapidly characterize a broad range of compositions, microstructures, and strain rates. This method, described in an earlier publication [20], is a powerful platform for rapid materials discovery as it circumvents the need for time-consuming and costly process optimization. A similar effort to properly characterize a single alloy composition and microstructure using traditional, macro-scale testing methods, like tensile testing, would require onerous process tuning to manufacture low defect density specimens [48]. However, as a counterpoint, scratch-based strength and fracture toughness measurements preclude decoupling of strain-hardening effects [49], and nanoindentation requires corrections for size effects (due to steep strain gradients associated with shallow indentation depths) [50] and tip geometry-dependent elastoplastic responses [46, 51]. This work is, in part, intended to highlight the untapped potential enabled by non-traditional combinations of materials and processing/characterization tools. The development of next-generation alloys that non-incrementally improve upon the state-of-the-art, as with Ni-based superalloys for high-temperature applications, may lie in similar efforts aimed at integrated development of materials and processing methods.

Results and discussion

Compositionally-graded Ni_xNb_{1-x} alloy

Composition and hardness measurement results for compositionally-graded Ni_xNb_{1-x} are summarized in Fig. 1. A representative topographical image of a 50 N scratch track is shown in Fig. 1a, illustrating how track width, which relates to hardness, changes as a function of composition along the specimen. Figure 1b shows average hardness values and atomic composition percentages for the majority of the scratch as a function of longitudinal position. Hardness values varied along the length of the scratch, peaking near the eutectic global composition ($Ni_{59.5}Nb_{40.5}$). The appearance of significant periodicity in scratch-hardness (Fig. 1b) as a function of wear track longitudinal position, parallel to the build direction, suggests a strong thermal history component, as the periodicity in hardness is comparable to the AM layer deposition thickness (both approximately 250 μm). At a wear track position of ≅ 4.1 mm, where composition was measured to be $Ni_{62}Nb_{38}$ (at.%), close to the eutectic [52], hardness reached $H \cong 17.1$ GPa. However, as discussed below, although this composition is generally a good glass former [53], there was no evidence of amorphous domains, but rather ordered orthorhombic δ-Ni_3Nb and rhombohedral μ-Ni_6Nb_7 intermetallic phases that were multimodal in size. The highest hardness value of $H \cong 19.5$ GPa occurred at an approximate wear track location of 5 mm, corresponding to an off-eutectic (Nb-deficient) composition of $Ni_{65}Nb_{35}$ (at.%). This is similar to work by Chen et al. [54], who found a similar two-phase structure using annealed arc-melted specimens.

Results of nanoindentation testing along the compositionally-graded Ni_xNb_{1-x} sample are shown in Fig. 1c. Indents were performed in 0.2 mm increments at locations adjacent to the scratch tracks, in an unworn location far enough away (see methods in Sect. 4.4) to avoid overlapping with work hardened zones. The average and standard deviation in hardness plotted in Fig. 1c correspond to measurements at indentation depths between 140 and 170 nm. Nanoindentation hardness values are generally in agreement with corresponding scratch data. The highest hardness from the nanoindentation occurred at a wear track position of ≅ 4.8 mm, with $H \cong 16$ GPa to 18 GPa, again corresponding to a composition range close to the global eutectic composition, where scratch hardness was $H \cong 17$ GPa to 20 GPa. Indentation hardness in a Nb-rich region ($H \cong 11$ GPa to 13 GPa, at a wear track position of ≅ 1 mm to 2 mm) was higher than scratch hardness ($H \cong 6$ GPa to 9 GPa); this difference can be attributed to microstructural heterogeneity and significant difference in the interaction volume of the nano-scale indentation and micro/macro-scale scratch methods, as well as the previously mentioned thermal history effects. Nevertheless, similar trends in hardness were found using both techniques; differences in hardness could be a result of real variation in hardness, or an aliasing artifact. Size effects, here meaning amplification of nanoindentation hardness at shallow depths, were shown to be negligible for indentation depths greater than about 120 nm. Following the method from Nix and Gao [50], the bulk or asymptotic hardness value H_0 was determined using depth-dependent hardness data for each location; an illustration of this analysis is shown in Fig. 1d near the location of maximum
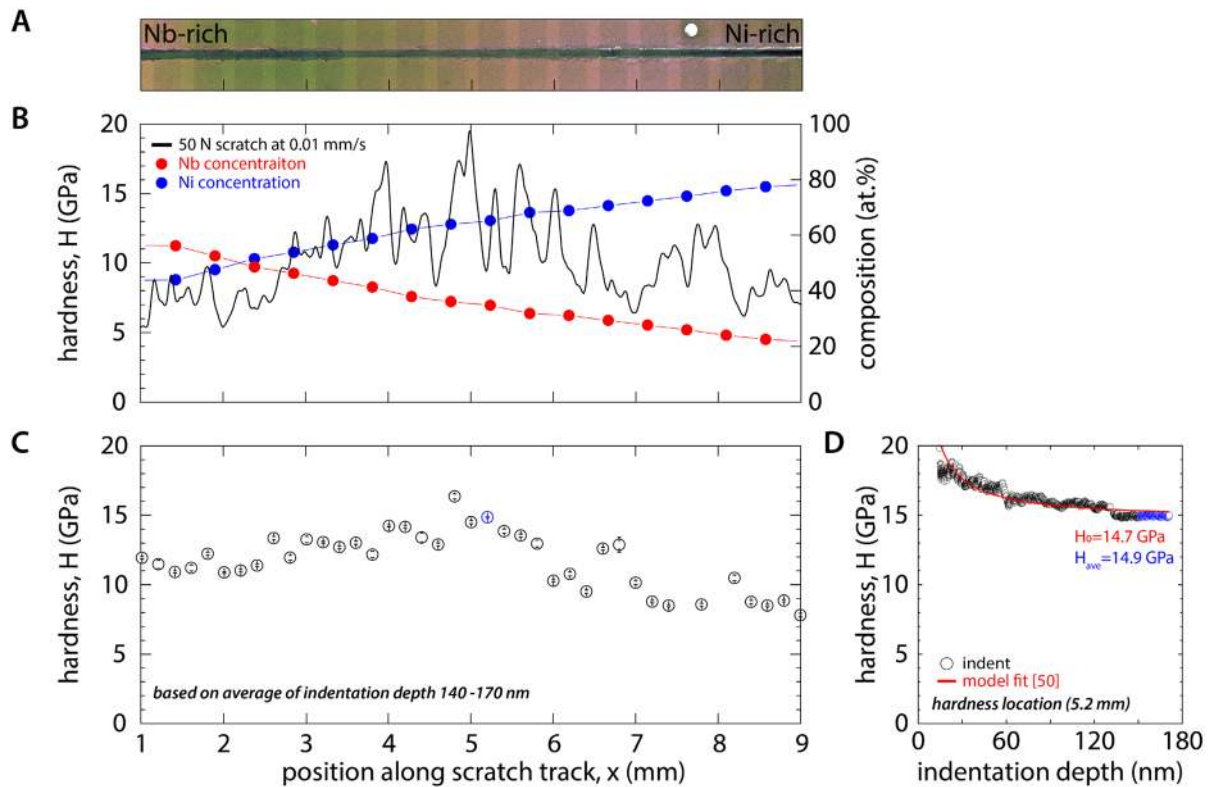
Figure 1: Mechanical and compositional properties of compositionally-graded Ni$_x$Nb$_{1-x}$ alloy. (A) Topographical image of a scratch track from the Nb-rich to the Ni-rich region. (B) Scratch-based hardness and composition measurements along a scratch track. (C) Nanoindentation hardness measurements along a scratch track (at depths from 140 to 170 nm); the blue symbol indicates the location that aligns most closely with the peak hardness scratch location and corresponds to the depth-dependent data in panel (D). (D) Nanoindentation hardness as a function of depth, average hardness between 140 and 170 nm, and fit of Nix and Gao model hardness in the limit of infinite depth, H_0 [50].

hardness where the composition was approximately Ni$_{66}$Nb$_{34}$. These data show good agreement with the model and corroborates the high hardness values measured by scratch testing.

Figure 2 shows large-area SEM micrographs of one representative scratch track for the compositionally-graded Ni$_x$Nb$_{1-x}$ specimen. The top image shows the Nb-rich end, where significant cracking was observed, with cracks spanning the width of the track and into adjacent regions. With increasing Ni concentration up to the eutectic composition (top two images), moving left-to-right, the width of the scratch tracks narrows corresponding to increasing hardness, with a minimum width and peak hardness near the center of the middle image. The near-eutectic region (middle image) was observed to have a microstructure distinct from the near-pure compositions, consisting of needle-like (1 to 10 μm wide, 10 s to 100 s μm long) δ-Ni$_3$Nb grains dispersed in a μ-Ni$_6$Nb$_7$ eutectic (lamellar) matrix (see additional characterization, below). The near-eutectic region showed only a few, small cracks, likely due to increased crack deflection and screening in the two-phase intermetallic, multimodal grain size structure (see microscopy results, below) [55]. Below about 25 at.% Nb (corresponding in the present case to the region shown in bottom image in Fig. 2), a transition to a two-phase FCC Ni

and ordered orthorhombic δ-Ni$_3$Nb structure is thermodynamically favored, with a second eutectic consisting of a Ni–Ni$_3$Nb lamellar structure [54]; this combination of phases explains the lower incidence of cracks, because of the higher ductility of the pure Ni or Ni-rich phase.

Representative surface SEM and EBSD inverse pole figure orientation and phase maps (Fig. 3a–c), pole figure (Fig. 3d), and cross-sectional STEM-HAADF images and chemical maps (Fig. 3e and f) for an undeformed (as-fabricated) location in the high-hardness, near-eutectic region are shown in Fig. 3. SEM and EBSD (Fig. 3a–c) show the multimodal, multiscale (10 s of nm to 10 s of μm) distribution of δ-Ni$_3$Nb grains and suggest an off-eutectic structure with coarse grained δ-Ni$_3$Nb phases within a finer eutectic (lamellar) matrix of δ-Ni$_3$Nb and μ-Ni$_6$Nb$_7$. STEM chemical analysis revealed the presence of an inclusion of η-NiNb$_2$O$_x$ [56], appearing near the bottom of the HAADF imagine in Fig. 3e and as a brighter region in the corresponding chemical map in Fig. 3f. The pole figure shown in Fig. 3d indicates a strong (~33×random) {001} texture for the δ-Ni$_3$Nb phase, interspersed in a matrix of eutectic lamellar (confirmed by STEM images (Fig. 3e and f)). The poorly indexed locations shown in black in Fig. 3b and c were below the spatial resolution of the EBSD rather than indicative of
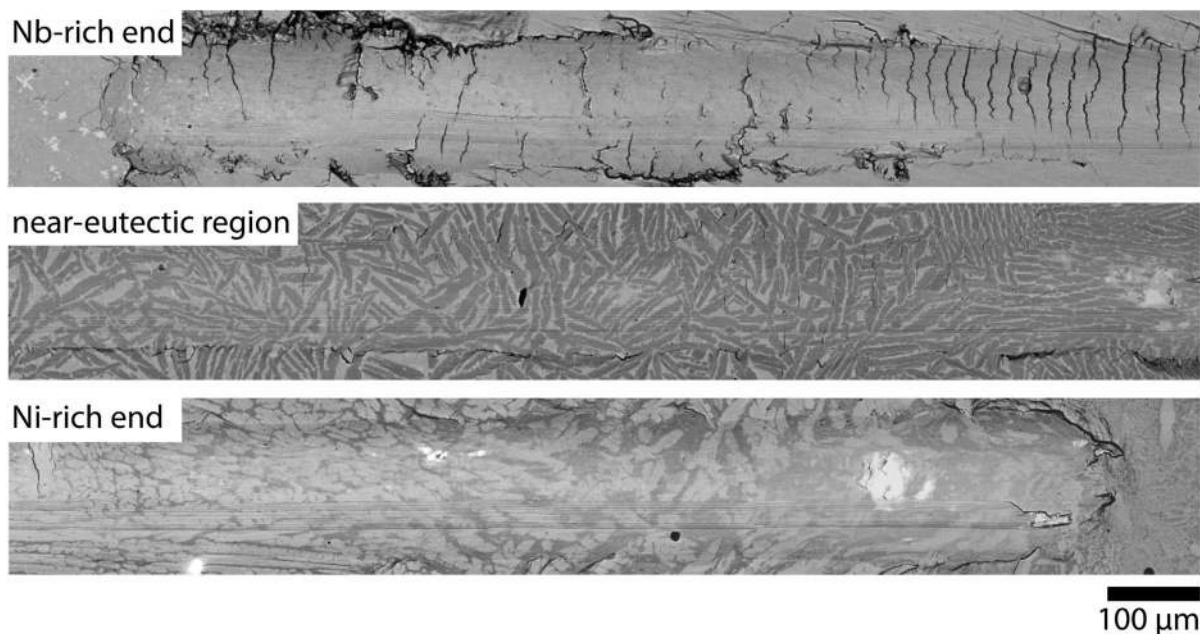
Figure 2: SEM back-scattered electron (SEM-BSE) micrographs of representative regions (Nb-rich, near-eutectic Ni–Nb mix, and Ni-rich) of the micro-scratch wear track on the compositionally-graded Ni_xNb_{1-x} alloy. Note the relative difficulty in resolving the wear track in the near-eutectic region, where the highest hardness was measured (see text). The scratch-based measurements were performed at a 0.01 mm/s sliding speed and 50 N normal load.

an amorphous structure. EBSD analysis showed little evidence of the metastable γ''-Ni_3Nb phase, though its existence cannot be completely ruled out with the current data. Cross-sectional high-resolution STEM images that were acquired from the peak hardness location along the centerline of the 0.01 mm/s scratch track are shown in Fig. 4. Significant changes were observed compared to an undeformed region (Fig. 3e), including significant refinement of both grains and phases, with 10 s of nm size grains near the surface, and a large concentration of planar defects (sub-grain boundaries) and incoherent nanotwins (Fig. 4b and c). The planar defects are reminiscent of the typically high-temperature shear bands, or possibly superlattice dislocations, that accommodate deformation in Ni-based superalloys [40] and Co-Al-W intermetallics [5]. Deformation of Laves intermetallic compounds, including μ-phases like Ni_6Nb_7, via synchroshear (a combination of shear-induced twinning and dislocation slip) was proposed by Kronberg [57] and the subject of an extensive recent investigation by Schröders et al. [58]. This mechanism may explain the prevalence of incoherent twin boundaries in the deformed μ-Ni_6Nb_7 crystal shown in Fig. 4c.

Uniform-composition of near-eutectic ($Ni_{59.5}Nb_{40.5}$) alloy

Representative SEM and EBSD orientation and phase maps (Fig. 5a–c), pole figure (Fig. 5d), and STEM-HAADF and EDS chemical mapping (Fig. 5e and f) for an undeformed

(as-fabricated) location on the single-composition, near-eutectic alloy are shown in Fig. 5. Similar to the compositionally-graded sample in the near-eutectic region, these images show the presence of a multimodal, multiscale distribution of δ-Ni_3Nb grains in a matrix of μ-Ni_6Nb_7 with sporadic inclusions of metastable $NiNb_2O_x$. Surprisingly, compared to the graded sample, there is an even stronger texture ($\sim 86 \times$ random) observed for the δ-Ni_3Nb phase found between the larger δ needle-like grains, and the overall grain size is skewed larger. These possibly indicate higher temperature during the AM process and/or lower thermal conductivity of the near-eutectic alloy. Diagonal striations in the brighter phase in the STEM-HAADF image (Fig. 5e) were determined to be planar defects in the μ-Ni_6Nb_7, that do not appear to bisect the δ-Ni_3Nb grains. Additionally, cross-sectional STEM of the δ-Ni_3Nb grains confirm that they are needle-like, i.e., with a cylindrical shape having rounded ends. STEM-EDS mapping (Fig. 6a) and a calculated atomic Ni/Nb ratio line profile across the phase boundary (Fig. 6b) suggest that the two phases were δ-Ni_3Nb and μ-Ni_6Nb_7. The atomic Ni/Nb ratio line profile shows some localized variability, indicating that the phases retained some degree of nanoscale chemical disorder and are not fully at thermodynamic equilibrium.

A summary of scratch test results for the single composition alloy is shown in Fig. 7. Hardness and fracture toughness are plotted as a function of strain rate (Fig. 7a). Hardness values ranged from 13.9 to 15.0 GPa, in good agreement with the (global) near-eutectic region in the compositionally-graded
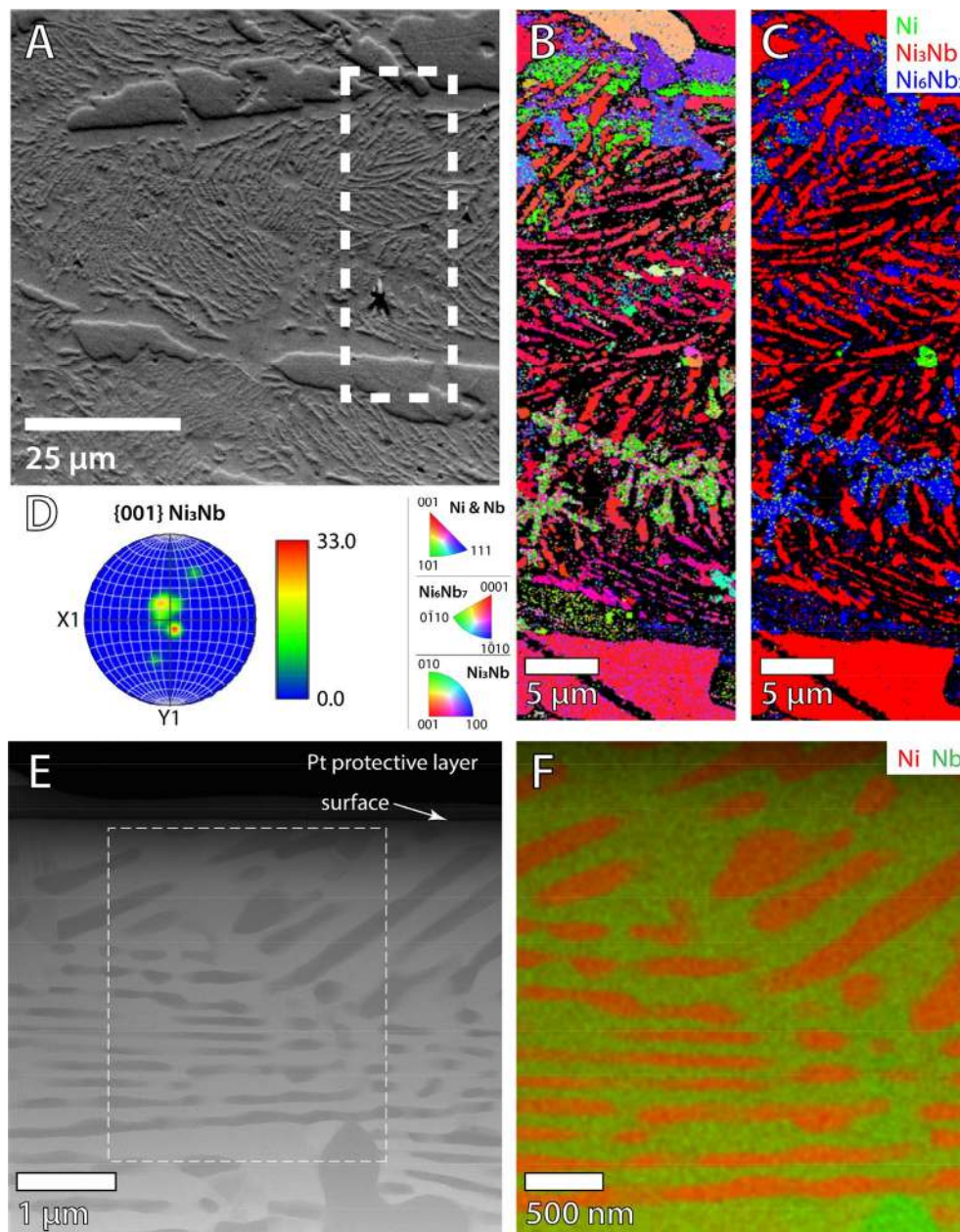
Figure 3: Characterization of the undeformed high hardness region of compositionally-graded Ni_xNb_{1-x} alloy. (A) SEM back-scattered electron (SEM-BSE) micrograph, (B) EBSD inverse pole figure orientation and (C) phase maps, (D) pole figure, (E) STEM-HAADF image of representative undeformed microstructure, and (F) corresponding STEM-EDS map showing primarily the presence of two distinct phases (δ-Ni_3Nb and μ-Ni_6Nb_7) with an inclusion of η-$NiNb_2O_x$ (bright green region near the bottom edge).

specimen. This comparison between samples, and the fact that the hardest region was in a Ni-rich composition, suggests that either (1) the combination of primary δ-Ni_3Nb with a Ni_3Nb/Ni_6Nb_7 eutectic matrix corresponds to higher hardness or (2) that this composition resulted in greater strengthening due a reduced initial grain size [59, 60] and eutectic lamellar spacing of the matrix [39] promoted by the rapid solidification of AM processing. A combination of both mechanisms is also possible. Fracture toughness values reported in Fig. 7a ranged

from $K_c \cong 70.8$–88.7 MPa $m^{1/2}$. This range of fracture toughness is commensurate with other nickel-based alloy systems, that have been reported to range between $K_c \cong 80$–100 MPa $m^{1/2}$ [44, 61–66]. Similarly, scratch-based determination of fracture toughness (treated as a mode II crack) was shown to match (within 10–20%) traditional (mode I) plane strain K_{IC} values for multiple polymers, ceramics and metals, including 2024-T4 and -T351 aluminum, 1045 and 1144 steel, and Ti-6Al-4 V [46].
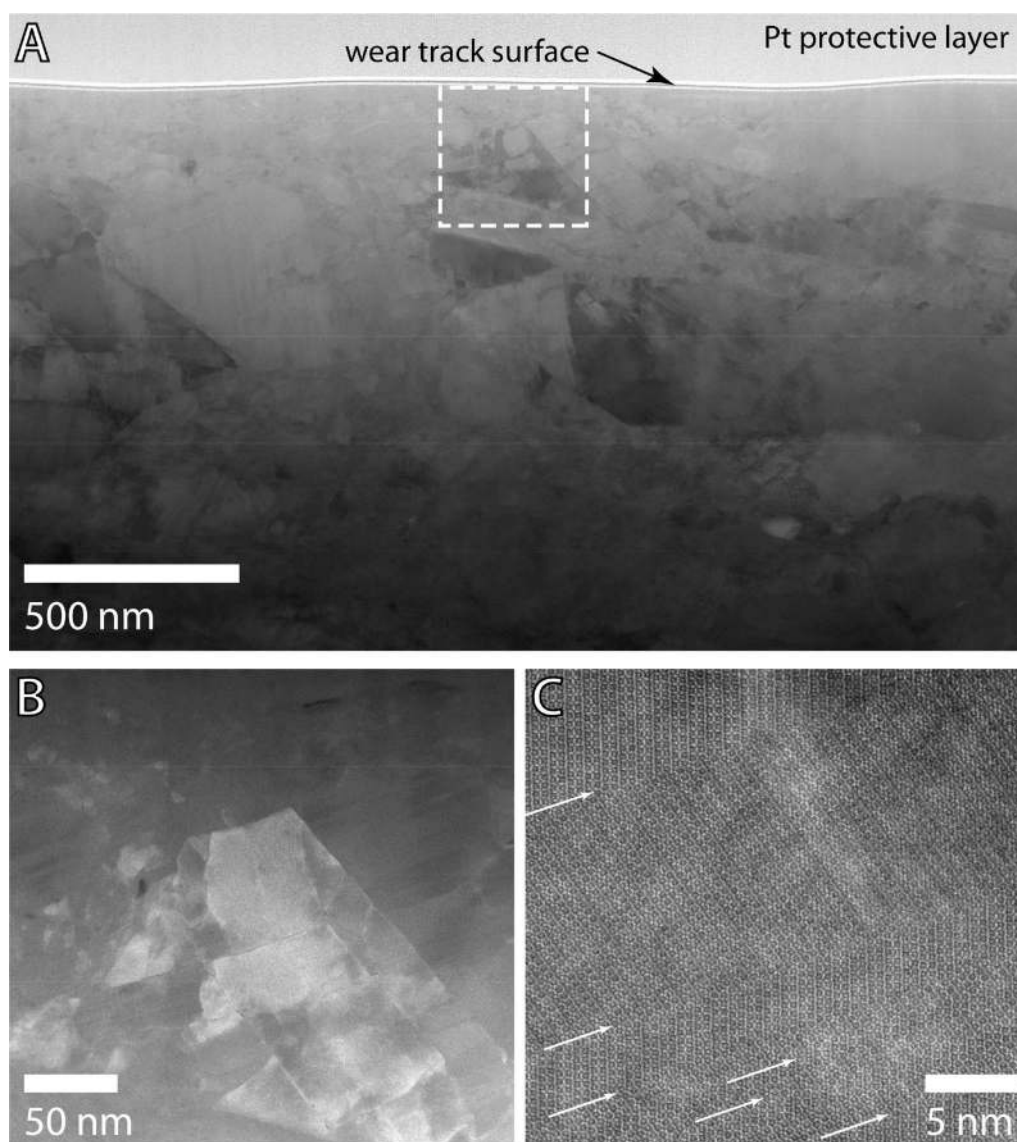
Figure 4: STEM analysis of in-track microstructure of compositionally-graded Ni_xNb_{1-x} alloy in high hardness region. (A) STEM bright field image showing evidence of a high density of sub-grain boundaries. (B) High-magnification STEM-HAADF highlighting the formation of sub-grain boundaries, and (C) atomic-resolution STEM-HAADF image of μ-Ni_6Nb_7 phase in [010] projection showing incoherent deformation-twin boundaries (white arrows).

Tiwary et al. [67] reported appreciable ductility (approximately 4%) with ternary Ni–Al-Zr intermetallic eutectic alloys, that they attributed to restriction of slip length and promotion of deformation twinning with nanocrystalline grain sizes. The evidence of retention of high strength at elevated temperature (2 GPa compressive yield strength at 700 °C) in Ni_{77}–Al_{12}–Zr_{11} (E1 crystal structure) shown by Tiwary et al. [67], coupled with the notable similarities in the microstructures and deformation behavior of our Ni–Nb alloys, suggest that similar behavior may be achievable with the two-phase (δ-Ni_3Nb and μ-Ni_6Nb_7) Ni–Nb system.

STEM bright-field and corresponding compositional EDS mapping along the centerline of a scratch track is shown in

Fig. 7b and c. A STEM bright-field image was used to better highlight nanocrystals present near the deformation surface (Fig. 7d). STEM of on-track microstructure shows evidence that scratch-based plastic deformation of the sample led to near-surface grain fragmentation, causing extreme grain refinement, as confirmed by EDS-STEM maps. Severe plastic deformation (SPD), as was imposed by the scratch method, is a well-established route to increasing strength of metals and alloys [68]. It is possible that the strength differences between scratch and nanoindentation, and the high hardness values in general, are primarily due to differences in the extent of work-hardening (i.e., differences in Hall–Petch and Taylor strengthening through the creation of interactions between dislocations
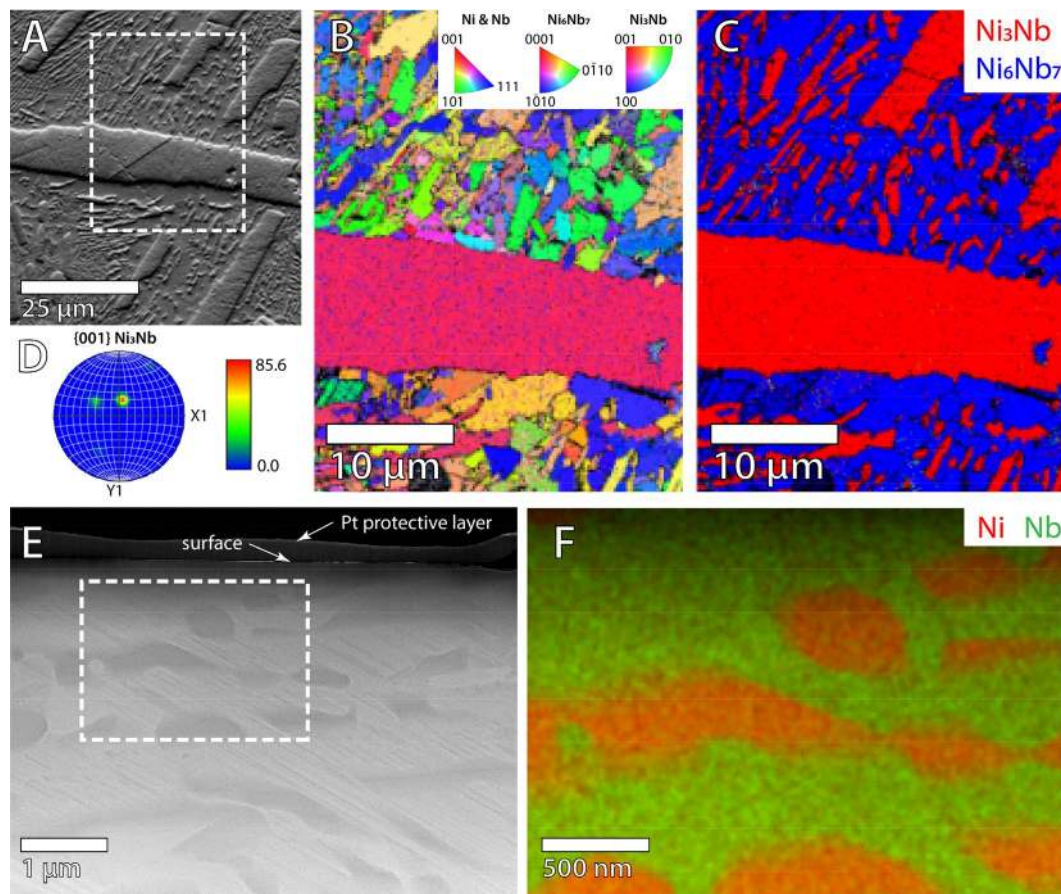
Figure 5: Characterization of the undeformed uniform-composition near-eutectic $Ni_{59.5}Nb_{40.5}$ alloy. (A) SEM back-scattered electron (SEM-BSE) micrograph, (B) EBSD inverse pole figure orientation and (C) phase maps, (D) pole figure, (E) STEM-HAADF image of representative microstructure, and (F) corresponding STEM-EDS map showing the presence of two distinct phases.

and grain boundaries [69, 70]). Higher total plastic deformation and work-hardening from scratch measurements, compared to nanoindentation, is expected since plastic deformation is proportional to penetration depth.

Strengthening mechanisms

Strain-rate sensitivity and activation volume were determined for the uniform-composition specimen, based on strain rate-dependent scratch hardness [71, 72]. The uniform-composition specimen is shown to have a relatively small strain-rate sensitivity of $m = 0.009 \pm 0.001$, similar to those reported by Chen et al. [73], for Ni–Nb metallic glassy films. In their study, they found that annealing the film for 60 min at 623 K resulted in a strain-rate sensitivity of $m = 0.0085$. Similarly, near zero strain-rate sensitivity was reported for a Ni-based superalloy at low temperature, while at room temperature, the value of strain-rate sensitivity value was measured to be $m = 0.0086$ [74]. In contrast, the strain-rate sensitivity of some coarse-grained intermetallic compounds (e.g., Cu_6Sn_5, Cu_3Sn, Cu_5Zn_8, Ag_3Sn, AgZn, and

Ag_5Zn_8) has been shown to be significantly higher than those measured here, with values reported in the range of $m \cong 0.082$ to 0.112 [75]. However, higher homologous temperature is associated with higher strain-rate sensitivity for coarser grain sizes, and these Sn-based alloys have a lower melting temperature than the two Ni–Nb-based intermetallic compounds here. Nanocrystalline Au-Cu alloys, with grain sizes in the range of 6 nm to 20 nm, were also determined to have comparably high strain rate sensitivities of $m \cong 0.1$ to 0.2, but measurement uncertainty was relatively high [72]. Fine-grained and nanocrystalline pure metals and dilute alloys have strain rate sensitivities that are smaller and weakly grain size-dependent [76], with values in the range of $m \cong 0.01$ to 0.05. The strain rate sensitivities for solid solutions, including high-entropy alloys, have been reported to be in the range of $m \cong 0.03$ to 0.2 [20, 77, 78]. Higher strain-rate sensitivity and small activation volumes are characteristics commonly associated with yield strengths that exhibit high temperature-sensitivity due to lattice friction (Peierls stress) and mechanisms including grain boundary sliding and superplasticity. Conversely, metallic glasses and crystalline metals that deform

Figure 6: (A) STEM-EDS map of the undeformed uniform-composition near-eutectic $Ni_{59.5}Nb_{40.5}$ alloy and (B) corresponding atomic Ni/Nb ratio line profile across phases, highlighting the presence of the two-phase δ-Ni_3Nb and μ-Ni_6Nb_7 microstructure.
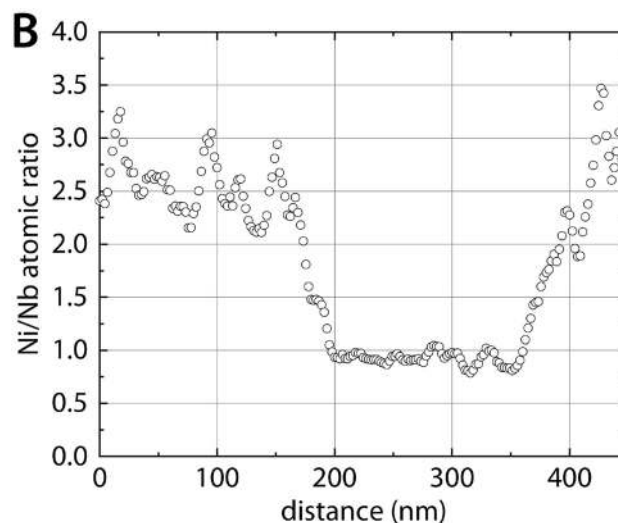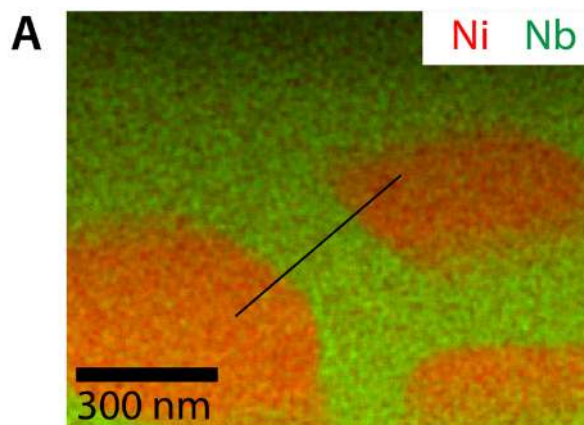
by shear-induced amorphization [43] typically have near-zero strain-rate sensitivities [79, 80], corresponding to non-diffusive, stress-activated inhomogeneous deformation.

Based on strain rate-dependent hardness, it was also possible to calculate an activation volume, $V = 0.16 \pm 0.02$ nm^3, comparable to those measured by Chen et al. [73], for annealed initially-glassy $Ni_{60}Nb_{40}$. The authors found a value of $V = 0.149$ nm^3 after a 60 min anneal at 623 K, well below the glass transition temperature of 841 K [81], such that the material remained glassy but achieved some degree of relaxation. Interestingly, hardness values for the glassy Ni–Nb annealed alloy only ranged from $H \cong 11.7$ GPa to 11.9 GPa [73], suggesting that bimodal crystalline intermetallic structures are substantially higher in hardness than the amorphous material. The combination of activation volumes comparable to those for localized flow in glasses and hardness values comparable to those of ultra-nanocrystalline intermetallics may be the result of a transition to grain boundary sliding [82] and possibly dynamic amorphization [43]. This interpretation also agrees with work by Basariya et al. [60], who reported similar strength values for intermetallic compounds with ultra-nanocrystalline

grain sizes, in the range of 10 nm to 50 nm. To our knowledge, only one report of nanoindentation on Ni–Nb amorphous alloy ribbons yielded hardness values as high as reported here. Lesz and Dercz reported a nanoindentation hardness of 15 GPa on initially amorphous $Ni_{62}Nb_{38}$, but did not provide details about the measurement or microstructural end state (i.e., it is unclear whether stress-induced crystallization and phase transformations occurred) [83]. A lower limiting case for the strength of Ni–Nb may be that of the metallic glass phase for the eutectic composition, which has a reported compressive yield strength at room temperature of 3.2 GPa [84]; the Tabor relationship [85] can be used to convert between hardness and uniaxial yield strengths, $\sigma_Y = H/3$, implying that the hardness should be close to 10 GPa. In contrast, our multiphase uniform composition AM bulk specimen showed a higher hardness of about 15 GPa. Given that stress-induced crystallization (i.e., structural, not chemical ordering, as the latter would require long-range diffusive motion) is expected during low temperature deformation of metallic glasses [86], it is possible that a nanoscale eutectic lamellar ultra-nanocrystalline grain Ni–Nb specimen could exhibit higher hardness by suppression of intragranular
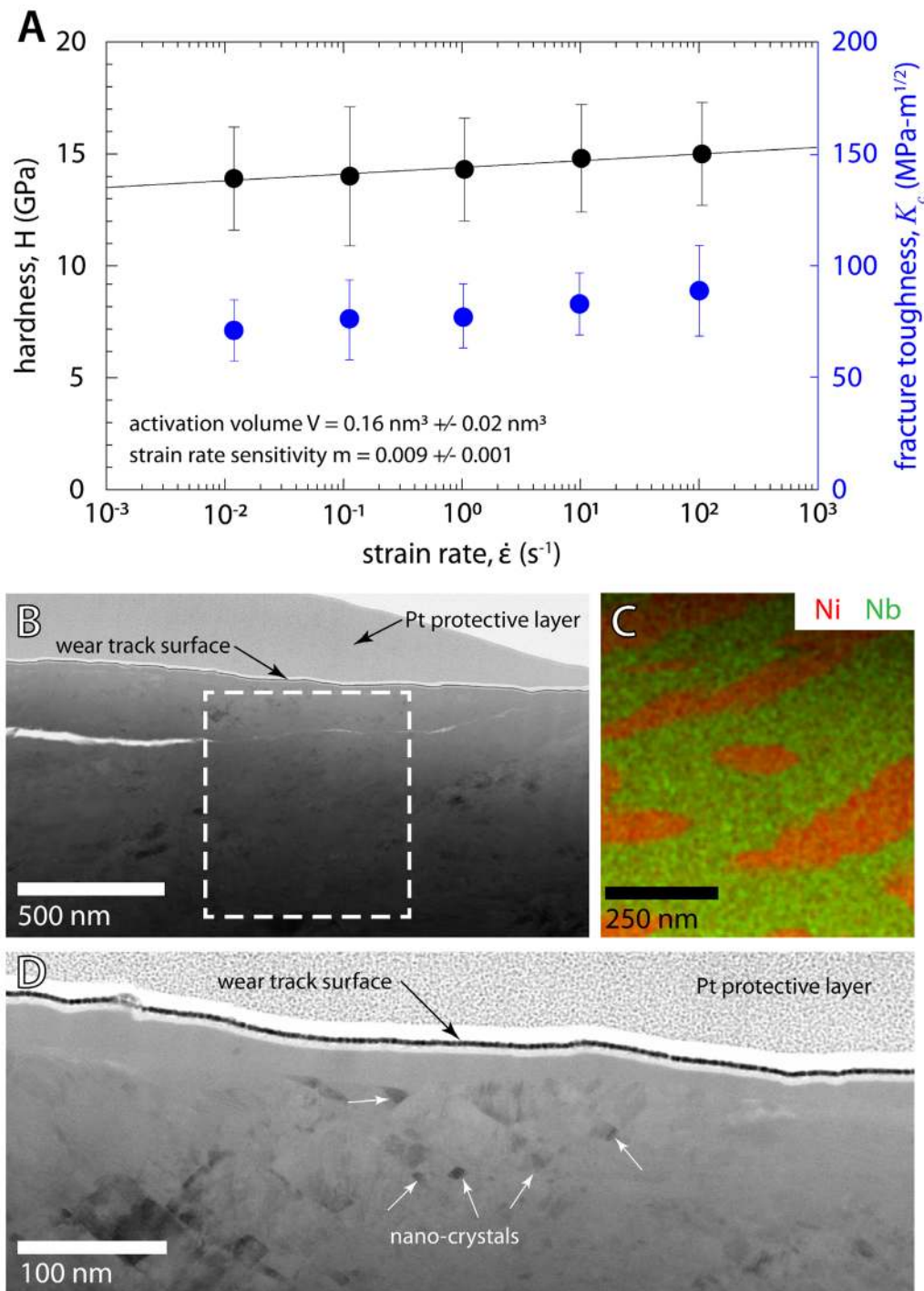
Figure 7: Mechanical and compositional properties of the uniform-composition near-eutectic $Ni_{59.5}Nb_{40.5}$ alloy. (A) Hardness (black circles) and fracture toughness (blue circles) as a function of strain rate. (B) Representative cross sectional in-track STEM bright field image along wear track centerline, (C) STEM-EDS map showing two distinct phases. (D) STEM bright field image highlighting in-track nanocrystals present after scratch deformation.

deformation. This could promote continuous, competing stress-driven amorphization and crystallization [43].

Microscopy analysis of scratch-hardness tracks showed evidence of 10–30 nm grains near the surface, corresponding to typical grain sizes at the crossover between Hall–Petch strengthening and inverse Hall–Petch softening [43, 87–90]. As an additional point of reference, hardness measurements on crystalline Ni–Nb specimens of varying composition and grain size showed a peak hardness of $H \cong 8.6$ GPa, for $Ni_{48}Nb_{52}$ [91] where SEM analysis also showed a lamellar eutectic structure

consisting of Ni_6Nb_7 and Ni_3Nb phases. These authors also measured the indentation hardness of isolated regions of Ni_6Nb_7 ($H \cong 7.6$ GPa) and Ni_3Nb ($H \cong 4.1$ GPa), using specimens with initial grain size in the 10 s of μm. This information suggests that the strength of our AM Ni–Nb specimens, consisting of a two-phase (δ-Ni_3Nb and μ-Ni_6Nb_7) multimodal distribution of grain and lamellar sizes, is likely due to a synergistic combination of solution and Hall–Petch strengthening, and possibly suppression of intracrystalline deformation/dislocation mechanisms. This applies to both the uniform composition and the graded material near the eutetctic composition. Metallic systems with comparable hardness have been reported by Nieh and Wang [59], who found 15–20 GPa nanoindentation hardness for Be with 2–10 at.% B with a grain size of about 20 nm, and Basariya et al., who reported indentation hardness for several nanocrystalline (10–50 nm grain size) intermetallic compounds, including TiAl, $NiAl_3$, $NbAl_3$, and Al_5Fe_2, in the range $H \cong 10 - 15$ GPa.

Summary and conclusions

The hardness and fracture toughness of AM-fabricated Ni–Nb specimens, both graded and uniform, near-eutectic compositions, were measured using scratch-based and nanoindentation techniques. A multimodal distribution of grain and cell sizes, spanning from a few nanometers to tens of micrometers, was observed via SEM and STEM microscopy. This work highlights the usefulness of AM methods to enable fabrication of parts made of traditionally brittle or otherwise difficult-to-process intermetallic compounds like δ-Ni_3Nb and μ-Ni_6Nb_7. Additionally, potential deformation and strengthening mechanisms were discussed. The highest hardness measurements, measured via scratch testing, corresponded to extreme near-surface grain refinement.

Comparisons of hardness, strain-rate sensitivity, and activation volume between metallic glasses and intermetallic compounds were used to explain the high strength of these materials and differences in strength between scratch and indentation. Differences in hardness between scratch and nanoindentation were explained in the context of defect-density dependent (e.g., Hall–Petch) strengthening mechanisms. Activation volumes and strain-rate sensitivity values indicate the possibility that extreme grain refinement led to suppression of intragranular deformation mechanisms and that the highest hardness values (in the near-eutectic composition region) may be linked to the mechanism of dynamic amorphization. This interpretation is supported by microscopy analysis showing that the initial microstructure included nanocrystalline grains interspersed between larger grains. The nanocrystallinity limits the possibility of intragranular deformation and promotes mechanisms like stress-induced amorphization (competing with crystallization

and grain growth), driving the system to the Hall–Petch/inverse Hall–Petch crossover.

Materials and methods

Fabrication and processing

Graded Ni_xNb_{1-x} and uniform, near-eutectic (nominal composition of $Ni_{59.5}Nb_{40.5}$) specimens were fabricated on an open-architecture laser-based directed-energy deposition (LB-DED) system equipped with a YLS-2000 laser operating at a wavelength of 1064 nm. The laser system is mounted to the spindle of a 3-axis Tormach CNC 770 housed in an inert Ar-filled glovebox. The inert environment was maintained at < 50 ppm O_2 and < 10 ppm H_2O during all builds. The powder feedstock was fluidized from individual powder hoppers via rotary feed wheels and Ar carrier gas toward the melt pool.

The process parameters used for both specimens consisted of a laser power of 500 W, scan speed of 400 mm/min, layer height of 0.2 mm, and an optic size of 1 mm. Both specimens were fabricated on a Ni 200 substrate with a temperature maintained at 12 °C via a contact heat exchanger with flowing refrigerated water. For the graded Ni_xNb_{1-x} specimen, eight layers of pure Ni were consolidated, followed by layer-wise increases in Nb content at approximately 1.02 at.% increments; a 100% Nb concentration was reached at about 98 layers, after which an additional eight layers of pure Nb were added, for a total of 114 layers.

Scanning electron microscopy, X-ray spectroscopy, and transmission electron microscopy

Both graded Ni_xNb_{1-x} and uniform near-eutectic thin wall specimens were mounted in a cold set epoxy and ground smooth using SiC paper. To achieve an optimal surface for microstructural analysis, the specimens were polished with a 1 μm diamond suspension followed by a two-step vibratory polish using a 0.3 μm Al_2O_3 and a 0.04 μm SiO_2 slurry. Scanning electron microscopy (SEM) was performed on a Zeiss Supra 55-VP FE-SEM equipped with Oxford Instruments X-Max SDD energy-dispersive X-ray spectroscopy (EDS) and Symmetry electron backscatter diffraction (EBSD) detectors. Backscatter- and secondary-electron images, EDS, and EBSD maps were collected with an acceleration voltage of 20 kV along a representative microscratch.

The graded and uniform specimens were further investigated by scanning transmission electron microscopy (STEM) on specimens prepared by focused ion beam (FIB). The microstructure was studied by STEM imaging using a high-angle annular dark-field (HAADF) detector and a bright-field detector as well as by STEM chemical analysis using EDS. Atomic composition of the alloys was calculated based on STEM-EDS maps by using

the Cliff and Lorimer method [92]. A FEI Titan™ G2 80-200 STEM with a Cs probe corrector and ChemiSTEM™ technology (X-FEG™ and SuperX™ EDS with four windowless silicon drift detectors) operated at 200 kV was used.

Scratch-based hardness and fracture toughness

Micro-scratch experiments were performed on the graded and uniform specimens using a Revetest RST[3] scratch tester. Detailed overviews of the experimental methods for determining hardness and strain-rate sensitivity can be found elsewhere [20, 72, 90, 93]. Composition-dependent hardness of the graded Ni_xNb_{1-x} sample and strain rate-dependent hardness of the $Ni_{59.5}Nb_{40.5}$ sample were determined by generating multiple wear tracks oriented parallel to the build plate direction at a constant 50 N contact force using a spheroconical diamond Rockwell indenter (radius $R = 200$ μm ± 10 μm and apex angle $\alpha = 120° ± 1°$). Five tracks with a length of 4 mm were generated on each sample at sliding speeds ranging from 10^{-3} to 10^1 mm/s in order-of-magnitude increments. On the graded Ni_xNb_{1-x} sample, 10 mm long tracks were used to capture a majority of the composition space. The beginning and ending 10% (1 mm each) of each track were omitted from analysis due to inertial effects. Tracks were spaced 3 mm apart to avoid strain hardening effects. The indenter tip was cleaned using a roughing cloth followed by an isopropyl alcohol rinse and determined to be clean and free of debris using an optical microscope before and after experiments, to ensure that no cracking or significant wear occurred during testing.

A Bruker Contour GT-I optical interferometer with a $10 \times$ Mirau objective was used to capture the entirety of each wear track via image stitching. This objective translated to a lateral resolution of 500 nm and a vertical resolution of < 1 nm. The wear track widths from the topographical scans were used to compute strain rate and hardness. In this study, strain rate was defined as $\dot{\varepsilon} = v/w$, where v is scratch velocity and w is average track width, and average scratch hardness was defined as $H = \frac{8}{\pi} \frac{F_n}{w^2}$ [72], where F_n is the normal or applied force. The strain-rate sensitivity exponent m and activation volume V were computed using data from experiments on the uniform-composition specimen. The strain-rate sensitivity exponent was calculated via the relationship $m = \frac{\partial \ln(H)}{\partial \ln(\dot{\varepsilon})}$ [72] and the activation volume was determined using the expression $V = 3\sqrt{3}k_B T \frac{\partial \ln(\dot{\varepsilon})}{\partial H}$, where k_B is the Boltzmann constant and T is the absolute temperature [90].

Fracture toughness was determined for the uniform-composition specimen from scratch data following the method in Akono *et al.* [94]. The maximum penetration depths d_p along the length of each scratch track were determined from the interferometric topographical scans, similar to the widths used to calculate hardness. The fracture toughness at each sliding speed

was then calculated using the expression $K_C = \frac{F_t}{\sqrt{2pA}}$, where K_C is the fracture toughness, F_t is the measured position-dependent friction force, and p and A are the perimeter length and projected semi-circular area of the contact. The perimeter length was defined as $p = 2R \arccos\left(\frac{R-d_p}{R}\right)$ where R is the indenter radius (200 μm), for depths of indentation smaller than the threshold value that would engage the conical portion of the tip (i.e., $d_p < 27$ μm). The projected contact area was calculated as $A = 0.5pR - \left(R - d_p\right)\sqrt{R^2 - \left(R - d_p\right)^2}$. Error in the reported fracture toughness values was associated with penetration depth variability along the scratch.

Nanoindentation

Nanoindentation experiments were performed with a Berkovich tip on a Hysitron TI-950 nanoindenter. The graded Ni_xNb_{1-x} specimen used for the scratch testing was subsequently used in the nanoindentation experiments. Indents were placed mid-way between scratch track centerlines, corresponding to a distance of 1.5 mm from adjacent scratch tracks to avoid work hardening effects and facilitate direct comparisons between scratch and indentation results, as well as more easily locate indents after testing. Prior to the Ni_xNb_{1-x} measurements, the tip area function and load frame compliance were calibrated over the entire load range of the instrument with fused silica as the reference material. For the Berkovich tip, the tip area function was defined as $A(h_c) = C_0 h_c^2 + C_1 h_c$, where h_c is the contact depth and C_0 and C_1 are coefficients related to tip shape [51]. Here, C_0 and C_1 were found through fits to the calibration data assuming a reduced modulus $E_r = 69.6$ GPa for diamond and fused silica [47]. These values were in good agreement with the area function model down to h_c of 20 nm to 30 nm. For the Ni_xNb_{1-x} measurements, a linear array of 500 indents was performed in load control to a maximum force of 11 mN. The indent spacing was 20 μm; small enough to facilitate high-resolution data across the specimen, but large enough to prevent interactions between neighboring indents [95]. For each indent, a CMX (continuous measurement of X) load function was utilized, consisting of a constant strain-rate load superimposed with a 110 Hz oscillating load. The strain rate was kept constant at 0.046 s^{-1} to mitigate strain-rate effects, and an oscillating load was utilized to provide depth-dependent data. From this loading scheme, the storage modulus E' was determined by $E' = k_s\sqrt{\pi}/2\sqrt{A}$, where k_s is the contact stiffness and A is the contact area. Similarly, the hardness H was calculated by $H = F_{max}/A$, where F_{max} is the maximum force and A is the contact area. E' and H were calculated as a function of both composition and depth, thereby facilitating one-dimensional (cross-sections) and two-dimensional (maps) representations of the data.

Acknowledgments

Data availability

Data available upon request.

Open Access

References

1. W.M. Tucho, P. Cuvillier, A. Sjolyst-Kverneland, V. Hansen, Microstructure and hardness studies of Inconel 718 manufactured by selective laser melting before and after solution heat treatment. Mater. Sci. Eng. A **689**, 220 (2017)

2. K.A. Christofidou, N.G. Jones, E.J. Pickering, R. Flacau, M.C. Hardy, H.J. Stone, The microstructure and hardness of Ni-Co-Al-Ti-Cr quinary alloys. J. Alloys Compd. **688**, 542 (2016)

3. H. Qi, M. Azer, A. Ritter, Studies of standard heat treatment effects on microstructure and mechanical properties of laser net shape manufactured Inconel 718. Metall. Mater. Trans. A **40**, 2410 (2009)

4. T. Zhou, H. Ding, X. Ma, W. Feng, H. Zhao, A. Li, Y. Meng, H. Zhang, Effect of precipitates on high-temperature tensile strength of a high W-content cast Ni-based superalloy. J. Alloys Compd. **797**, 486 (2019)

5. T.M. Pollock, Alloy design for aircraft engines. Nat. Mater. **15**, 809 (2016)

6. M.C. Chaturvedi, Y. Han, Strengthening mechanisms in Inconel 718 superalloy. Met. Sci. **17**, 145 (1983)

7. J.M. Oblak, D.F. Paulonis, D.S. Duvall, Coherency strengthening in Ni base alloys hardened by DO22 Γ′ precipitates. Metall. Trans. **5**, 143 (1974)

8. X. You, Y. Tan, S. Shi, J.M. Yang, Y. Wang, J. Li, Q. You, Effect of solution heat treatment on the precipitation behavior and strengthening mechanisms of electron beam smelted Inconel 718 superalloy. Mater. Sci. Eng. A **689**, 257 (2017)

9. L. Kovarik, R.R. Unocic, J. Li, P. Sarosi, C. Shen, Y. Wang, M.J. Mills, Microtwinning and other shearing mechanisms at intermediate temperatures in Ni-based superalloys. Prog. Mater. Sci. **54**, 839 (2009)

10. K. Kawagishi, A. Yeh, T. Yokokawa, T. Kobayashi, Y. Koizumi, H. Harada, *Superalloys 2012*, vol. 189 (Seven Springs, Warrendale, 2012)

11. A. Gilchrist, T.M. Pollock, K.J. Hemker, D.M. Dimiduk, H. Clemens, R. Darolia, H. Inui, J.M. Larsen, V.K. Sikka, M. Thomas, *Structural Intermetallics*, vol. 3 (TMS, Warrendale, 2001)

12. F. Saint-Antonin, W. Lefebvre, I. Blum, Niobium base superalloys: achievement of a coherent ordered precipitate structure in the Nb solid-solution. Crystals **9**, 345 (2019)

13. B.P. Bewlay, M.R. Jackson, H.A. Lipsitt, The balance of mechanical and environmental properties of a multielement niobium-niobium silicide-based in situ composite. Metall. Mater. Trans. A **27**, 3801 (1996)

14. S. Drawin, J.P. Monchoux, J.L. Raviart, A. Couret, Microstructural properties of Nb-Si Based alloys manufactured by powder metallurgy. Adv. Mater. Res **278**, 533–538 (2011)

15. C. Seemüller, M. Heilmaier, T. Hartwig, M. Mulser, N. Adkins, M. Wickins, Influence of microstructure and processing on mechanical properties of advanced Nb-silicide alloys. MRS Online Proc. Libr. **1516**, 317 (2013)

16. O.P. Shaboldo, Y.M. Vitorskii, V.V. Sagaradze, E.G. Volkova, Effect of heat treatment on the fine structure and properties of a niobium-base superalloy. Phys. Met. Metallogr. **117**, 1281 (2016)

17. M. Fujikura, A. Kasama, R. Tanaka, S. Hanada, Effect of alloy chemistry on the high temperature strengths and room temperature fracture toughness of advanced Nb-based alloys. Mater. Trans. **45**, 493 (2004)

18. R. Tanaka, A. Kasama, M. Fujikura, I. Iwanaga, H. Tanaka, Y. Matsumura, Newly developed niobium-based superalloys for

elevated temperature application. Miner. Met. Mater. Soc. **2**, 89 (2004)

19. J.J. Lewandowski, M. Seifi, Metal additive manufacturing: a review of mechanical properties. Annu. Rev. Mater. Res. **46**, 151 (2016)

20. M.A. Melia, S.R. Whetten, R. Puckett, M. Jones, M.J. Heiden, N. Argibay, A.B. Kustas, High-throughput additive manufacturing and characterization of refractory high entropy alloys. Appl. Mater. Today **19**, 100560 (2020)

21. L.E. Murr, S.M. Gaytan, D.A. Ramirez, E. Martinez, J. Hernandez, K.N. Amato, P.W. Shindo, F.R. Medina, R.B. Wicker, Metal Fabrication by additive manufacturing using laser and electron beam melting technologies. J. Mater. Sci. Technol. **28**, 1 (2012)

22. J.H. Martin, B.D. Yahata, J.M. Hundley, J.A. Mayer, T.A. Schaedler, T.M. Pollock, 3D printing of high-strength aluminium alloys. Nature **549**, 365 (2017)

23. T. Peng, K. Kellens, R. Tang, C. Chen, G. Chen, Sustainability of additive manufacturing: an overview on its energy demand and environmental impact. Addit. Manuf. **21**, 694 (2018)

24. T.F. Babuska, M.A. Wilson, K.L. Johnson, S.R. Whetten, J.F. Curry, J.M. Rodelas, C. Atkinson, P. Lu, M. Chandross, B.A. Krick, J.R. Michael, N. Argibay, D.F. Susan, A.B. Kustas, Achieving high strength and ductility in traditionally brittle soft magnetic intermetallics via additive manufacturing. Acta Mater. **180**, 149–157 (2019)

25. A.B. Kustas, D.F. Susan, K.L. Johnson, S.R. Whetten, M.A. Rodriguez, D.J. Dagel, J.R. Michael, D.M. Keicher, N. Argibay, Characterization of the Fe-Co-1.5V soft ferromagnetic alloy processed by laser engineered net shaping (LENS). Addit. Manuf. **21**, 41 (2018)

26. J.W. Pegues, M.A. Melia, R. Puckett, S.R. Whetten, N. Argibay, A.B. Kustas, Exploring additive manufacturing as a high-throughput screening tool for multiphase high entropy alloys. Addit. Manuf. **37**, 101598 (2020)

27. J.M. Torralba, M. Campos, High entropy alloys manufactured by additive manufacturing. Metals (Basel) **10**, 1 (2020)

28. W. Chen, Z. Li, Boyer RBT-AM for the AI, 11—additive manufacturing of titanium aluminides, in *Additive Manufacturing for the Aerospace Industry*. ed. by F. Froes (Elsevier, New York, 2019), pp. 235–263

29. W.E. Frazier, Metal additive manufacturing: a review. J. Mater. Eng. Perform. **23**, 1917 (2014)

30. M.M. Attallah, R. Jennings, X. Wang, L.N. Carter, Additive manufacturing of Ni-based superalloys: the outstanding issues. MRS Bull. **41**, 758 (2016)

31. S.P. Murray, K.M. Pusch, A.T. Polonsky, C.J. Torbet, G.G.E. Seward, N. Zhou, S.A.J. Forsik, P. Nandwana, M.M. Kirka, R.R. Dehoff, W.E. Slye, T.M. Pollock, A defect-resistant Co–Ni superalloy for 3D printing. Nat. Commun. **11**, 1 (2020)

32. Y.H. Zhou, Z.H. Zhang, Y.P. Wang, G. Liu, S.Y. Zhou, Y.L. Li, J. Shen, M. Yan, Selective laser melting of typical metallic

materials: an effective process prediction model developed by energy absorption and consumption analysis. Addit. Manuf. **25**, 204 (2019)

33. Y. Brif, M. Thomas, I. Todd, The use of high-entropy alloys in additive manufacturing. Scr. Mater. **99**, 93 (2015)

34. S. Luo, C. Zhao, Y. Su, Q. Liu, Z. Wang, Selective laser melting of dual phase AlCrCuFeNix high entropy alloys: formability, heterogeneous microstructures and deformation mechanisms. Addit. Manuf. **31**, 100925 (2020)

35. P. Agrawal, S. Thapliyal, S.S. Nene, R.S. Mishra, B.A. McWilliams, K.C. Cho, Excellent strength-ductility synergy in metastable high entropy alloy by laser powder bed additive manufacturing. Addit. Manuf. **32**, 101098 (2020)

36. L. Deng, S. Wang, P. Wang, U. Kühn, S. Pauly, Selective laser melting of a Ti-based bulk metallic glass. Mater. Lett. **212**, 346 (2018)

37. Z. Mahbooba, L. Thorsson, M. Unosson, P. Skoglund, H. West, T. Horn, C. Rock, E. Vogli, O. Harrysson, Additive manufacturing of an iron-based bulk metallic glass larger than the critical casting thickness. Appl. Mater. Today **11**, 264 (2018)

38. W. Wu, J. Jiang, G. Li, J.Y.H. Fuh, H. Jiang, P. Gou, L. Zhang, W. Liu, J. Zhao, Ultrasonic Additive manufacturing of bulk Ni-based metallic glass. J. Non. Cryst. Solids **506**, 1 (2019)

39. J.M. Park, K.B. Kim, W.T. Kim, M.H. Lee, J. Eckert, D.H. Kim, High strength ultrafine eutectic Fe-Nb-Al composites with enhanced plasticity. Intermetallics **16**, 642 (2008)

40. R.W. Kozar, A. Suzuki, W.W. Milligan, J.J. Schirra, M.F. Savage, T.M. Pollock, Strengthening mechanisms in polycrystalline multimodal nickel-base superalloys. Metall. Mater. Trans. A Metall. Mater. Sci. **40**, 1588 (2009)

41. H.A. Roth, C.L. Davis, R.C. Thomson, Modeling solid solution strengthening in nickel alloys. Metall. Mater. Trans. A **28**, 1329 (1997)

42. Z.C. Cordero, B.E. Knight, C.A. Schuh, Six decades of the Hall-Petch effect—a survey of grain-size strengthening studies on pure metals. Int. Mater. Rev. **61**, 495 (2016)

43. M. Chandross, N. Argibay, Ultimate strength of metals. Phys. Rev. Lett. **124**, 125501 (2020)

44. E.P. George, D. Raabe, R.O. Ritchie, High-entropy alloys. Nat. Rev. Mater. **4**, 515 (2019)

45. J.R. Trelewicz, C.A. Schuh, The Hall–Petch breakdown in nanocrystalline metals: a crossover to glass-like deformation. Acta Mater. **55**, 5948 (2007)

46. A.-T.T. Akono, F.-J.J. Ulm, Scratch test model for the determination of fracture toughness. Eng. Fract. Mech. **78**, 334 (2011)

47. W.C. Oliver, G.M. Pharr, Measurement of hardness and elastic modulus by instrumented indentation: advances in understanding and refinements to methodology. J. Mater. Res. **19**, 3 (2004)

48. B.C. Salzbrenner, J.M. Rodelas, J.D. Madison, B.H. Jared, L.P. Swiler, Y.L. Shen, B.L. Boyce, High-throughput stochastic

tensile performance of additively manufactured stainless steel. J. Mater. Process. Technol. **241**, 1 (2017)

49. P. Zhang, S.X. Li, Z.F. Zhang, General relationship between strength and hardness. Mater. Sci. Eng. A **529**, 62 (2011)

50. W.D. Nix, H. Gao, Indentation size effects in crystalline materials: a law for strain gradient plasticity. J. Mech. Phys. Solids **46**, 411 (1998)

51. W.C. Oliver, G.M. Pharr, An improved technique for determining hardness and elastic modulus using load and displacement sensing indentation experiments. J. Mater. Res. **7**, 1564 (1992)

52. M. Leonhardt, W. Löser, H.G. Lindenkreuz, Solidification kinetics and phase formation of undercooled eutectic Ni–Nb melts. Acta Mater. **47**, 2961 (1999)

53. L. Xia, W.H. Li, S.S. Fang, B.C. Wei, Y.D. Dong, Binary Ni–Nb bulk metallic glasses. J. Appl. Phys. **99**, 26103 (2006)

54. H. Chen, Y. Du, H. Xu, Y. Liu, J.C. Schuster, Experimental investigation of the Nb-Ni phase diagram. J. Mater. Sci. **40**(6019), 6022 (2005)

55. R.W. Steinbrech, Toughening mechanisms for ceramic materials. J. Eur. Ceram. Soc. **10**, 131 (1992)

56. P.Y. Lee, C.C. Koch, The formation and thermal stability of amorphous Ni–Nb alloy powder synthesized by mechanical alloying. J. Non. Cryst. Solids **94**, 88 (1987)

57. M.L. Kronberg, Plastic Deformation of single crystals of sapphire: basal slip and twinning. Acta Metall. **5**, 507 (1957)

58. S. Schröders, S. Sandlöbes, B. Berkels, S. Korte-Kerzel, On the structure of defects in the Fe 7 Mo 6 μ-phase. Acta Mater. **167**, 257 (2019)

59. T.G. Nieh, J.G. Wang, Hall-Petch relationship in nanocrystalline Ni and Be-B alloys. Intermetallics **13**, 377 (2005)

60. M.R. Basariya, N.K. Mukhopadhyay, S. Sripathi, K.A. Padmanabhan, Grain size softening effect in intermetallics. J. Alloys Compd. **673**, 199 (2016)

61. B. Gludovatz, A. Hohenwarter, D. Catoor, E.H. Chang, E.P. George, R.O. Ritchie, A fracture-resistant high-entropy alloy for cryogenic applications. Science **345**, 1153 (2014)

62. N.R. Moody, R.E. Stoltz, M.W. Perra, The effect of hydrogen on fracture toughness of the Fe-Ni-Co superalloy IN903. Metall. Trans. A **18**, 1469 (1987)

63. X. Yu, X. Lin, F. Liu, L. Wang, Y. Tang, J. Li, S. Zhang, W. Huang, Influence of post-heat-treatment on the microstructure and fracture toughness properties of Inconel 718 fabricated with laser directed energy deposition additive manufacturing. Mater. Sci. Eng. A **798**, 140092 (2020)

64. R. Firoz, S.K. Basantia, N. Khutia, H.N. Bar, S. Sivaprasad, G.V.S. Murthy, J. Alloys Compd. **845**, 156276 (2020)

65. M. J. Sippel, Tensile and Fracture Toughness Behavior of Waspaloy., (1983).

66. I. S. Hwang, R. G. Ballinger, M. M. Morra, and M. M. Steeves, Mechanical properties of Incoloy 908—an update. In Materials. Springer, New York (1992), pp. 1–10.

67. C. Tiwary, V.V. Gunjal, D. Banerjee, K. Chattopadhyay, Intermetallic eutectic alloys in the Ni-Al-Zr system with attractive high temperature properties. MATEC Web Conf. **14**, 01005 (2014)

68. R. Valiev, Nanostructuring of metals by severe plastic deformation for advanced properties. Nat. Mater. **3**, 511 (2004)

69. A. Argon, *Strengthening Mechanisms in Crystal Plasticity*, vol. 4 (Oxford University Press on Demand, Oxford, 2008)

70. G.I. Taylor, The mechanism of plastic deformation of crystals. Part I.—Theoretical. Proc. R. Soc. Lond. Ser. A Contain. Pap. a Math. Phys. Charact. **145**, 362 (1934)

71. T.J. Rupert, J.R. Trelewicz, C.A. Schuh, Grain boundary relaxation strengthening of nanocrystalline Ni-W alloys. J. Mater. Res. **27**, 1285 (2012)

72. L.O. Nyakiti, A.F. Jankowski, Characterization of strain-rate sensitivity and grain boundary structure in nanocrystalline gold-copper alloys. Metall. Mater. Trans. A Phys. Metall. Mater. Sci. **41**, 838 (2010)

73. H. Chen, Y.X. Song, T.H. Zhang, M. Wu, Y. Ma, Structure relaxation effect on hardness and shear transformation zone volume of a Ni–Nb metallic glassy film. J. Non. Cryst. Solids **499**, 257 (2018)

74. K. Gopinath, A.K. Gogia, S.V. Kamat, R. Balamuralikrishnan, U. Ramamurty, Tensile properties of Ni-based superalloy 720Li: temperature and strain rate effects. Metall. Mater. Trans. A **39**, 2340 (2008)

75. J.M. Song, Y.L. Shen, C.W. Su, Y.S. Lai, Y.T. Chiu, Strain Rate dependence on nanoindentation responses of interfacial intermetallic compounds in electronic solder joints with Cu and Ag substrates. Mater. Trans. **50**, 1231 (2009)

76. Q. Wei, S. Cheng, K.T. Ramesh, E. Ma, Effect of nanocrystalline and ultrafine grain sizes on the strain rate sensitivity and activation volume: Fcc versus Bcc metals. Mater. Sci. Eng. A **381**, 71 (2004)

77. J.Y. He, C. Zhu, D.Q. Zhou, W.H. Liu, T.G. Nieh, Z.P. Lu, Steady state flow of the FeCoNiCrMn high entropy alloy at elevated temperatures. Intermetallics **55**, 9 (2014)

78. M. Sadeghilaridjani, S. Muskeri, V. Hassannaeimi, M. Pole, S. Mukherjee, Strain rate sensitivity of a novel refractory high entropy alloy: intrinsic versus extrinsic effects. Mater. Sci. Eng. A **766**, 138326 (2019)

79. A. Bhattacharyya, G. Singh, K. Eswar Prasad, R. Narasimhan, U. Ramamurty, On the strain rate sensitivity of plastic flow in metallic glasses. Mater. Sci. Eng. A **625**, 245 (2015)

80. C.A. Schuh, T.C. Hufnagel, U. Ramamurty, Mechanical behavior of amorphous alloys. Acta Mater. **55**, 4067 (2007)

81. Y. Ma, J.H. Ye, G.J. Peng, D.H. Wen, T.H. Zhang, Loading rate effect on the creep behavior of metallic glassy films and its correlation with the shear transformation zone. Mater. Sci. Eng. A **622**, 76 (2015)

82. N. Argibay, M. Chandross, S. Cheng, J.R. Michael, Linking Microstructural evolution and macro-scale friction behavior in metals. J. Mater. Sci. **52**, 2780 (2017)

83. S. Lesz, G. Dercz, Study on crystallization phenomenon and thermal stability of binary Ni–Nb amorphous alloy. J. Therm. Anal. Calorim. **126**, 19 (2016)

84. Z. Zhu, H. Zhang, D. Pan, W. Sun, Z. Hu, Fabrication of binary Ni–Nb bulk metallic glass with high strength and compressive plasticity. Adv. Eng. Mater. **8**, 953 (2006)

85. D. Tabor, A simple theory of static and dynamic hardness. Proc. R. Soc. London. Ser. A. Math. Phys. Sci. **192**, 247 (1948)

86. Y. Mao, J. Li, Y.C. Lo, X. Qian, E. Ma, Stress-driven crystallization via shear-diffusion transformations in a metallic glass at very low temperatures. Phys. Rev. B Condens. Matter Mater. Phys. **91**, 1 (2015)

87. M. Dao, L. Lu, R.J. Asaro, J.T.M. De Hosson, E. Ma, Toward a quantitative understanding of mechanical behavior of nanocrystalline metals. Acta Mater. **55**, 4041 (2007)

88. J.R. Weertman, D. Farkas, K. Hemker, H. Kung, M. Mayo, R. Mitra, H. Van Swygenhoven, Structure and mechanical behavior of bulk nanocrystalline materials. MRS Bull. **24**, 44 (1999)

89. M.R. Basariya, V.C. Srivastava, N.K. Mukhopadhyay, Inverse Hall-Petch like behaviour in a mechanically milled nanocrystalline Al5Fe2 intermetallic phase. Philos. Mag. **96**, 2445 (2016)

90. T.J. Rupert, J.C. Trenkle, C.A. Schuh, Enhanced solid solution effects on the strength of nanocrystalline alloys. Acta Mater. **59**, 1619 (2011)

91. C.R.M. Afonso, K. Martinez-Orozco, V. Amigó, C.A. Della Rovere, J.E. Spinelli, C.S. Kiminami, Characterization, corrosion resistance and hardness of rapidly solidified Ni–Nb alloys. J. Alloys Compd. **829**, 154529 (2020)

92. G. Cliff, G. Lorimer, The quantitative analysis of thin specimens. J. Microsc. **103**, 203 (1975)

93. A.R. Hinkle, J.F. Curry, H. Lim, B.L. Nation, M.R. Jones, P. Lu, N. Argibay, M. Chandross, Low Friction in BCC metals via grain boundary sliding. Phys. Rev. Mater. **4**, 63602 (2020)

94. A.T. Akono, N.X. Randall, F.J. Ulm, Experimental determination of the fracture toughness via microscratch tests: application to polymers, ceramics, and metals. J. Mater. Res. **27**, 485 (2012)

95. P. Sudharsha Pnhani, W.C. Oliver, A Critical Assessment of the effect of indentation spacing on the measurement of hardness and modulus using instrumented indentation testing. Mater. Des. **164**, 107563 (2019)